Imaging the emergence and natural progression of spontaneous autoimmune diabetes

James F. Mohan[a], Rainer H. Kohler[b], Jonathan A. Hill[a,1], Ralph Weissleder[b,c,2], Diane Mathis[a,2], and Christophe Benoist[a,2]

[a]Division of Immunology, Department of Microbiology and Immunobiology, Harvard Medical School, Boston, MA 02115; [b]Center for Systems Biology, Massachusetts General Hospital, Boston, MA 02114; and [c]Department of Systems Biology, Harvard Medical School, Boston, MA 02115

Contributed by Christophe Benoist, July 20, 2017 (sent for review May 4, 2017; reviewed by Kevan C. Herold and Roland M. Tisch)

Type 1 diabetes in the nonobese diabetic mouse stems from an infiltration of the pancreatic islets by a mixed population of immunocytes, which results in the impairment and eventual destruction of insulin-producing β-cells. Little is known about the dynamics of lymphocyte movement in the pancreas during disease progression. Using advanced intravital imaging approaches and newly created reporter mice (*Flt3-BFP2, Mertk-GFP-DTR, Cd4-tdTomato, Cd8a-tdTomato*), we show that the autoimmune process initiates first with a T cell infiltration into the islets, where they have restricted mobility but reside and are activated in apposition to CX3CR1$^+$ macrophages. The main expansion then occurs in the connective tissue outside the islet, which remains more or less intact. CD4$^+$ and CD8$^+$ T cells, Tregs, and dendritic cells (DCs) are highly mobile, going along microvascular tracks, while static macrophages (MF) form a more rigid structure, often encasing the islet cell mass. Transient cell–cell interactions are formed between T cells and both MFs and DCs, but also surprisingly between MFs and DCs themselves, possibly denoting antigen transfer. In later stages, extensive islet destruction coincides with preferential antigen presentation to, and activation of, CD8$^+$ T cells. Throughout the process, Tregs patrol the active compartments, consistent with the notion that they control the activation of many cell types.

diabetes | autoimmunity | immunoregulation

Type 1 diabetes (T1D) is an organ-specific autoimmune disease, schematically comprised of two phases: (*i*) an occult phase of pancreatic inflammation that reduces the number and function of insulin-producing β-cells, eventually provoking sufficient damage to result in (*ii*) the overt phase of diabetes, when insulin production is insufficient for proper glucose homeostasis. The genetics of T1D in mice and humans are very similar (1), with an overwhelming dominance of class II genes of the MHC that points to a primary dysfunction in tolerance and immunoregulation of CD4$^+$ T cells. The inflammatory infiltrate, however, involves a wide array of cell types, lymphoid as well as myeloid (2).

Much of what is known pertaining to the molecular and cellular events that precede T1D development have been uncovered using the nonobese diabetic (NOD) mouse, a highly informative model that shares many genetic and cellular features with the human disease. In NOD mice, sparse autoreactive T cells infiltrate islets beginning around 3–5 wk of age. Insulitis becomes well-established by 10–12 wk, incorporating a variety of cell types, several of which actively contribute to the progression to diabetes [e.g., NK cells, B cells, macrophages (MFs), and dendritic cells (DCs)] (3–6), or protect against it (Tregs, MFs again) (7–10). These cells can occasionally organize into tertiary lymphoid structures (11). Importantly, insulitis variably affects different islets, heavily infiltrated islets coexisting with fully intact and functional ones, as in humans (12–16). Overt diabetes eventually ensues in these mice between 12 and 30 wk of age.

A significant hurdle hampering the study of T1D is the nonsynchronous progression of insulitis and diabetes development. In addition to noninvasive but low-resolution imaging (7), static evaluations of islet infiltration and cellular composition have been provided by immunohistochemistry or flow cytometry, but neither can appreciate the dynamics of the lesions and the interactions between cells. Thus, how rogue T cells invade islets, how exactly complex and long-lived insulitic lesions are established, and what cellular interactions drive β-cell destruction remain largely enigmatic. Intravital time-lapse microscopy (IVM), by providing high-resolution and dynamic information, represents an attractive approach to tackle some of these questions. In the context of diabetes, it has been applied in a limited fashion because of the technical and logistical difficulties of visualizing the autoimmune response directly within the pancreas. Other than studies of isolated or transplanted islets (17–21), two studies have reported real-time imaging of islet infiltration in the intact pancreas (22, 23). Both involved the transfer of antigen-specific CD4$^+$ or CD8$^+$ T cells, that were acutely activated (either in vitro before transfer, or after transfer by virus-induced stimulation in vivo). One study showed that, as insulitis progressed, the motility of islet-specific T cells increased, with fewer stable interactions with antigen-presenting cells (APC) (23). The other showed, in an acute-onset model, that activated and islet-specific CD8$^+$ T cells could migrate freely in and out of islets, and could interact with and directly kill β-cells (22). Whereas these studies illuminated the dynamic nature of pancreatic infiltrates, such acute transfer models do not really recapitulate the natural course of spontaneous T1D over the weeks or months of progression.

Thus, we set out to use IVM to capture the natural emergence of the polyclonal autoimmune attack in the pancreas of NOD mice, without acute cell transfers or ectopic antigen expression. To capture the variety of cell types at play, we developed a versatile panel of reporter mice on the NOD genetic background, which could be intercrossed to track multiple types of immunocytes. In parallel, we developed IVM approaches that avoided physiologic disturbance (constant temperature, intact perfusion) and that allowed us to image the pancreas over hours

Significance

Dynamics and interactions of immunocytes infiltrating the pancreas during the natural progression of autoimmune diabetes are largely unknown. The construction of diabetes-prone nonobese diabetic mice with a panel of fluorescent reporters that illume infiltrating cells of the innate and adaptive immune systems, combined with intravital imaging of the pancreas, provide novel perspectives on the autoimmune process and on the ballet between aggressive and regulatory cells.

Author contributions: J.F.M., R.W., D.M., and C.B. designed research; J.F.M., R.H.K., and J.A.H. performed research; J.F.M., J.A.H., R.W., D.M., and C.B. analyzed data; and J.F.M. and C.B. wrote the paper.

Reviewers: K.C.H., Yale University; and R.M.T., University of North Carolina at Chapel Hill.

The authors declare no conflict of interest.

[1] Present address: Surface Oncology, Cambridge, MA 02139.

[2] To whom correspondence may be addressed. Email: rweissleder@mgh.harvard.edu, dm@hms.harvard.edu, or cb@hms.harvard.edu.

This article contains supporting information online at www.pnas.org/lookup/suppl/doi:10.1073/pnas.1707381114/-/DCSupplemental.

at a time at cellular resolution, and to extract multiplex volumetric data in a systematic and quantitative fashion. Using these tools, we evaluated the cellular dynamics of the autoimmune lesion at various stages of diabetes progression, spanning from the installation of the early insulitis through advanced destruction. The results suggest that, after being initiated by CD4$^+$ T cells first activated inside the islets, the lesions progress mainly in their periphery as a complex multicellular ensemble in which T cells interact with both DCs and MFs, culminating in most advanced forms in which CD8$^+$ T cells seem to be predominantly active.

Results

An IVM Platform to Track Spontaneous Autoimmunity in the Pancreas. We reasoned that, to image the spontaneous development of autoimmune diabetes dynamically and at cellular resolution, two new experimental approaches would have to be combined. First, we implemented and optimized a minimally invasive surgical procedure for exteriorization and stabilization of the pancreas during intravital imaging (Fig. 1*A*; detailed in *Materials and Methods*). Briefly, the pancreas of an anesthetized mouse was surgically exteriorized, carefully preserving all vascularization and connective tissue anchors. The live tissue was placed in a heated saline bath of Ringer's solution to maintain temperature, under the 20× objective of a confocal/multiphoton microscope set for time-lapse imaging. With this set-up, we were able to image the pancreas with full cell viability, mobility, and interactions for periods of several hours.

Second, we incorporated fluorescent tracers into the system without the potential disruptions linked to short-term cell transfers; in addition, we needed the ability to simultaneously image cells of several lineages to observe their interactions. To this end, we used CRISPR-based genome editing to knock in DNA segments

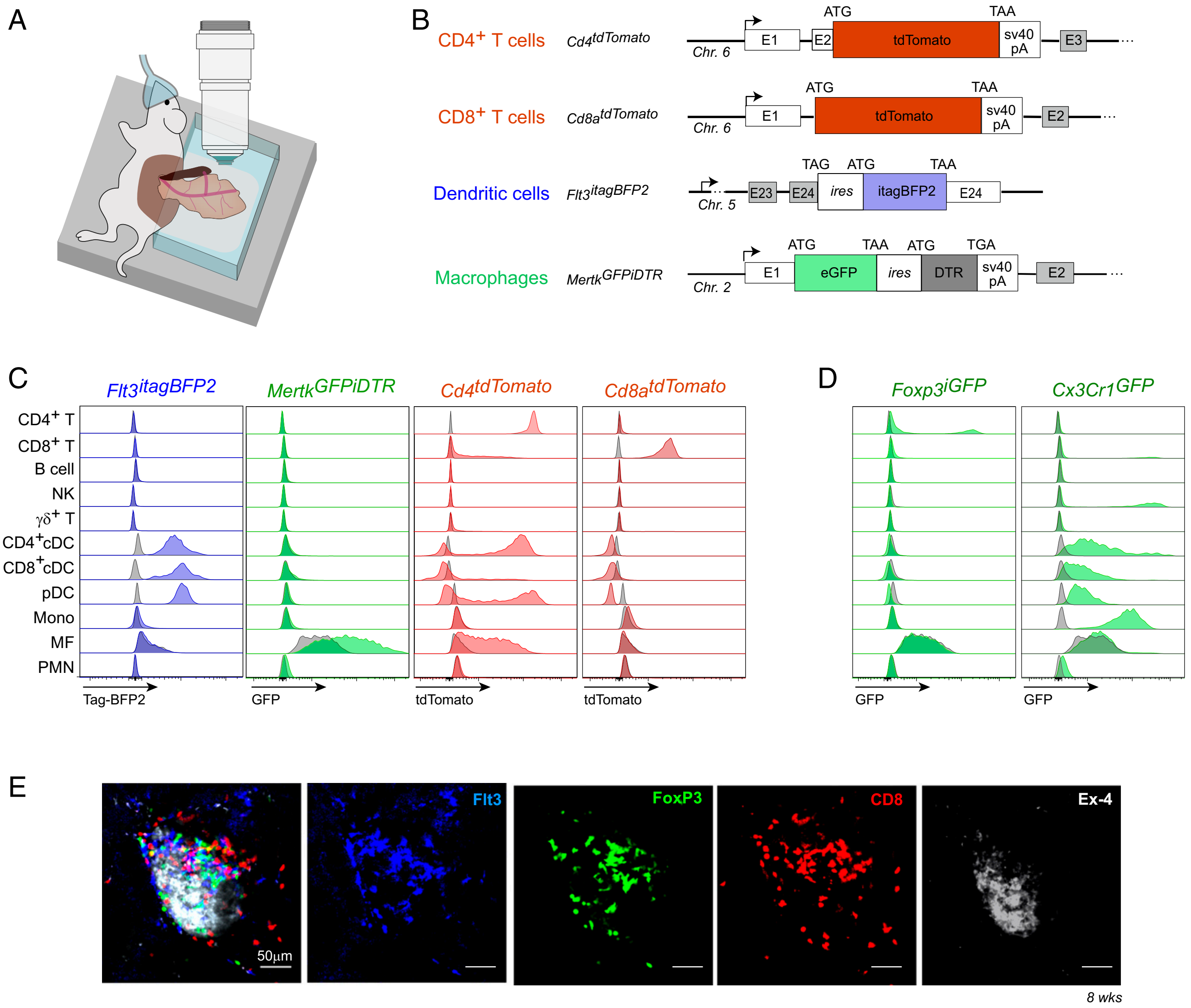

Fig. 1. Intravital imaging of immune cell dynamics within the pancreatic infiltrate during disease progression. (*A*) Overview of the intravital imaging set-up for exteriorized pancreas. (*B*) Schematic of reporter insertions into the *CD4*, *CD8a*, *Flt3*, and *Mertk* loci in NOD mice generated by CRISPR/Cas9 germline engineering. (*C*) Histograms depicting fluorescent protein expression among various splenocyte populations from 6-wk-old *Flt3-BFP2* (blue), *Mertk-GFP* (green), *Cd4-tdTomato* (red), and *Cd8a-tdTomato* (red) compared with negative controls (gray). Gating strategies for individual populations detailed in *SI Materials and Methods*. (*D*) Reporter expression in *Foxp3-GFP* (green) and *CX3CR1-GFP* (green) splenocyte populations compared with negative controls (gray). (*E*) Representative IVM image of an infiltrated islet in an 8-wk-old female CD8-Foxp3-Flt3 trireporter mouse injected with Ex-4 SeTau 647.

encoding several fluorescent reporters [tagBFP2 (hereafter BFP2), GFP, and tdTomato] into loci with specific expression in DCs, MFs, and CD4$^+$ and CD8$^+$ T cells (*Flt3*, *Mertk*, *Cd4*, and *CD8a*, respectively). For *Mertk*, an ires-DTR cassette was also included (Fig. 1*B*). These constructs were created by coinjection of Cas9 mRNA and single-guide RNAs (sgRNA) to cleave the genome at the desired position, and of engineered DNA fragments to drive resealing of the cuts by homologous recombination (24) (full description in *SI Materials and Methods*). These injections were performed directly into NOD embryos to avoid lengthy backcrosses. As illustrated in Fig. 1*C* and Fig. S1*A*, the resulting lines showed the expected patterns of expression at high levels in the desired cell-types and mid-to-low expression in other cells: *Flt3-BFP2* was expressed exclusively in DCs, *Cd4-tdTomato* in some DCs and MFs, and also low expression within a minor population of CD8$^+$ T cells, likely corresponding to recent thymic emigrants. *Mertk-GFP* expression was restricted to MFs, in which it showed some heterogeneity, as expected from the range of *Mertk* mRNA levels in different MFs (ImmGen database). This heterogeneity was particularly true of islet-resident MFs, which were more readily visualized using the *CX3CR1-GFP* reporter (25) than with the *Mertk-GFP* reporter. We also complemented these new reporter lines with a well-characterized *Foxp3-GFP* Treg reporter (26). Both the *Foxp3-GFP* and *Cx3cr1-GFP* lines were backcrossed onto the NOD genome for >10 generations. Importantly, the reporter constructs did not significantly affect the incidence of diabetes in the knockin lines, (Fig. S1*B*) (*P* = NS) nor the numbers and proportions of infiltrating cells. These lines were then intercrossed, allowing simultaneous tracking of up to four cell types, in some cases combining the same fluorochrome to detect nonoverlaping cell types. For example, intercrossing *Cd4-tdTomato*, *Foxp3-GFP*, *Mertk-GFP*, and *Flt3-BFP2* mice, resulted in red CD4$^+$ T cells, red and green (yellow) Tregs, green MFs, and blue DCs. To detect β-cells, we complemented the transgenic reporters by injecting, shortly before imaging, our previously described fluorescent exendin-4–like neopeptide conjugate that binds to the β-cell surface with high specificity (27). Preliminary imaging experiments showed that the diverse cell types could be detected in the infiltrated pancreas (Fig. 1*E*).

This system was then applied to image natural progression of diabetes. The observations described below encompass data from 143 animals imaged, most in the 3–5 or 8–12 wk of age timeframes, at the initiation of autoimmune infiltration or in conditions of well-established insulitis, respectively. Given the well-known asynchrony in the progression of insulitis in the islets of individual animal (referred to as “pancreatic vitiligo” by George Eisenbarth), NOD females around 12 wk of age presented with a range of lesions, using classic definition to parse “peri-insulitis” or “established insulitis” (islet-retaining spherical morphology and most infiltrating immunocytes confined to the outside) vs. “destructive insulitis” (contorted morphology of remaining β-cells with penetrating mass of infiltrate). We will discuss separately results from the periods of initial (around 5 wk) and established insulitis periods.

The Early Lesion. We first analyzed cell infiltrates at the initiation of pancreatic autoimmunity (3–5 wk of age). At this time, rare T cells could be observed deep within the islet and in the surrounding connective tissue (Fig. 2*A*). Islet-embedded cells included conventional CD4$^+$ and to a lesser extent CD8$^+$ T cells and Tregs. The proportion of islets harboring such lymphocytes increased with age, especially that of T cells present on the outside (Fig. 2*B*); indeed, the more the total number of islet-associated T cells increased, the more they were found outside the islets (Fig. 2*C*). The rare islet-infiltrating cells were not, at least at the 3-wk time point, a unique property of NOD mice, as they were also observed at very early times in diabetes-resistant F1 offspring of an intercross with C57BL/6 mice (Fig. 2*D*). However, the F1s did not show the numeric increase observed at 5 wk in NOD mice, nor the expanding localization outside the islets (Fig. 2*E*).

We then analyzed the behavior of T cells in these two locations, which proved very different. Those in the surrounding tissue migrated freely in the connective tissue along the outside perimeter of the islet (in some movies, in the *z*-plane above the islet) (Fig. 2 *F* and *G* and Movies S1 and S2). In contrast, those that localized within the islet exhibited highly restricted mobility in terms of mean velocity and overall displacement. This dichotomy applied to all T cell types, whether conventional CD4$^+$ or CD8$^+$ T cells, or Tregs. This comparatively low mobility of intraislet lymphocytes could be explained by different tissue architectures, tight junctions within the islets inhibiting movement, or by stable interactions with APCs. Indeed, long-lived interactions were observed with CX3CR1-GFP$^+$ MFs inside the islets (Fig. 3 *A* and *B* and Movies S3 and S4), and essentially all islet-infiltrating CD4$^+$ and CD8$^+$ T cells were engaged in such stable contacts (Fig. 3*B*), suggesting that presentation of islet-derived antigens is occurring given that these MFs constitutively sample β-cell granules for presentation to T cells (28, 29). In keeping with this notion, T cells from isolated islets showed clear up-regulation of CD69 and CD25, indicating recent activation through T cell receptor (TCR) engagement (Fig. 3*C*). Many intraislet CD4$^+$ T cells produced IFN-γ (Fig. 3*D*), supporting the notion that these are proinflammatory and potentially pathogenic cells.

The faster-moving T cells surrounding the islets had fewer contacts with APCs, although they did engage in transient associations. Contacts with MFs tended to be more prolonged than those with DCs (Fig. 3*E*). T cells in the islet-surrounding areas also associated closely with the microvasculature (visualized by injection of an intravascular tracer in Fig. 3*F*), and their mobility paths closely followed the vascular pattern (Fig. 3*F*, *Right*, Fig. S2, and Movie S5). These observations suggest that these extraislet T cells interact with, and track along, endothelial cells of MFs in the microvascular beds, much as they follow the network of fibroblastic reticular cells in lymph nodes (LN) (30). It is unknown whether these migration patterns are dependent on chemokine cues, as for LN T cells, or simply that the microvascular area is the most permissive space for T cells to migrate through.

Communication between the two compartments (inside/outside) of the early autoimmune lesion was then addressed. Over the course of observing many islets during this project, we observed occasional instances of T cells traversing the basement membrane (five instances, involving one or two T cells, in ≈25 islets examined for this particular aspect), illustrated in Fig. 3*G* and Movie S6. In most cases, the cells were moving from the outside in (Fig. 3*G*). Thus, while the two pools of cells exhibited different behaviors and did not exchange freely, they were not completely insulated.

The Advanced Lesion. We next analyzed the established lesions of 10- to 12-wk-old NOD females, most of which are destined to progress to diabetes. Images of established, florid insulitis were observed, with the usual large assemblage of hematopoietic cells congregating in the immediate vicinity of an islet (Fig. 4*A* and Movies S7 and S8), which they can completely overrun in the more extensive forms of destructive insulitis. Both DCs and MFs were found in these established insulitic lesions, often mixed in the same areas, but also with some more segregated areas that were predominantly populated by DCs or MFs (Fig. 4*A*, *Left*). The latter created, in the cases of more extensive infiltration, an impressive encapsulation of the islet perimeter, where MFs occupied more than half of the islet area in some images (Fig. 4*B*, Lower, and Fig. S3).

The two myeloid subsets showed markedly different mobility. The majority of DCs migrated very actively (Fig. 4*C* and Movie S8), albeit not quite as fast as T cells (1.9 ± 0.05 μm/min vs. 6.1 ± 0.42 μm/min for CD4$^+$ T cells). They followed clearly directional tracks over the 30- to 45-min period of observation (Fig. 4*C*,

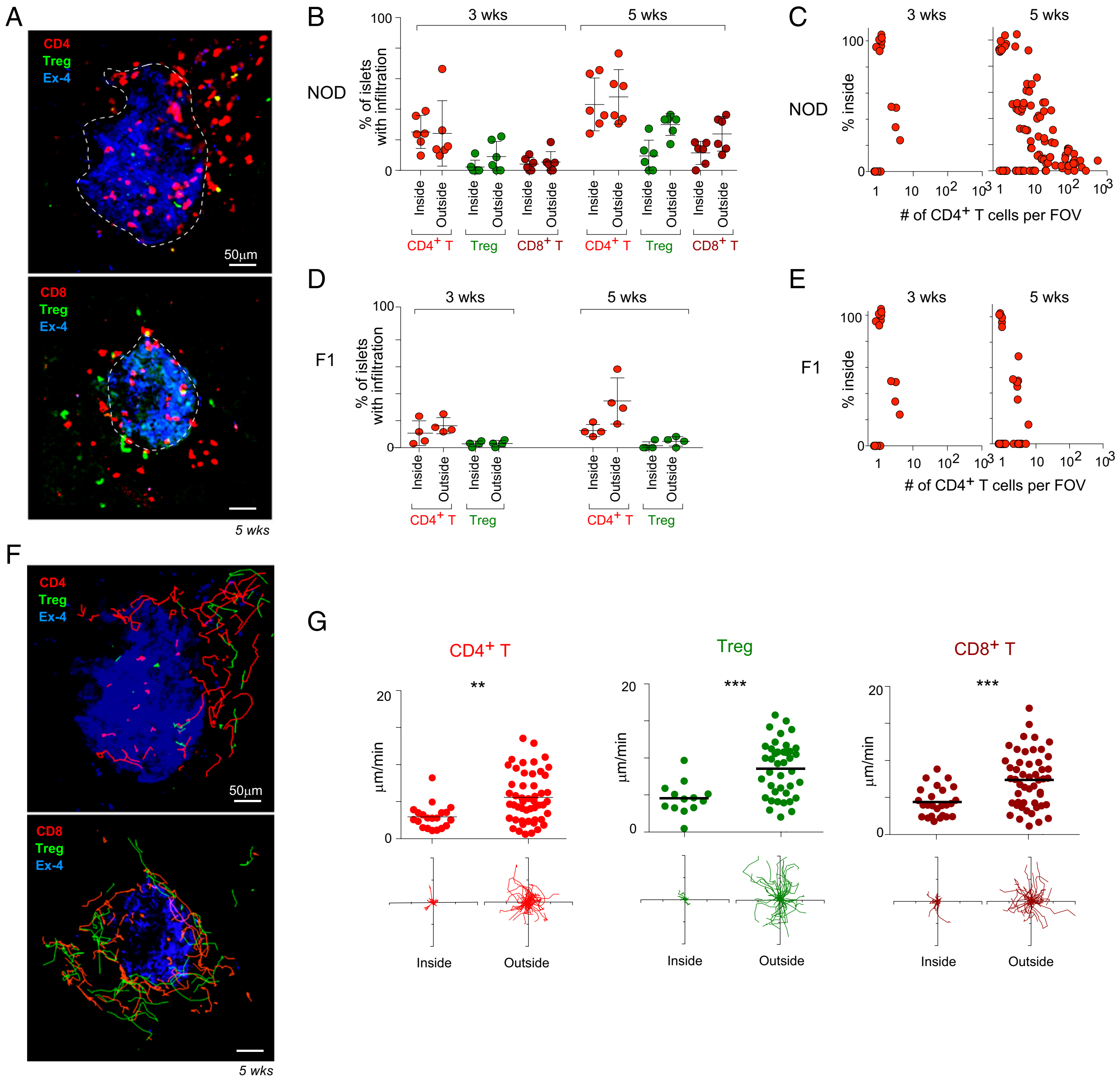

Fig. 2. Monitoring early T cell infiltration into the pancreas. (*A*) Representative IVM images of infiltrating T cells in 5-wk-old female *Cd4-tdTomato/Foxp3-GFP* and *Cd8a-tdTomato/Foxp3-GFP* reporter mice showing the localization of infiltrating T cells both inside and outside of the islet (delineated by dotted lines). (*B*) Quantitation of islet infiltration from ex vivo imaging of pancreata from 3- and 5-wk-old female *Cd4-tdTomato/Foxp3-GFP* and *Cd8a-tdTomato/Foxp3-GFP* mice. Each dot represents an individual mouse. (*C*) Frequency of $CD4^+$ T cells that localize within islets vs. the total number of T cells present within the corresponding lesion of infiltrated islets in 3- and 5-wk-old female *Cd4-tdTomato* reporter mice. Each dot represents an individual islet, data pooled from four to six mice. (*D*) Quantitation of islet infiltration from ex vivo imaging of pancreata from 3- and 5-wk-old F1 (B6 × NOD) *CD4-tdTomato/Foxp3-GFP* females. Each dot represents an individual mouse. (*E*) Frequency of $CD4^+$ T cells that localize within islets vs. the total number of T cells present within the corresponding lesion of infiltrated islets in 3- and 5-wk-old female F1 (B6xNOD) *Cd4-tdTomato* reporter mice. Each dot represents an individual islet, data pooled from four to six mice. (*F*) Representative images depicting the migratory tracks for CD4 T cells (*Upper*, red lines) CD8 T cells (*Lower*, red lines) and Tregs (green lines) over the course of imaging. Data correspond with cells depicted in *A*. (*G*) Quantitation of cellular velocities and displacement profiles for T cells segregated based on location inside or outside of the islet. Flower plots represent migration over 10 min. (Scale bar, 100 μm.). Data pooled from three to five mice (5-wk-old) per cell type. Error bars, SD. $^{**}P < 0.005$; $^{***}P < 0.0005$.

Right). A proportion of DCs were immobile, as were essentially all MFs (Fig. 4*C*), and only on the rarest occasions was a MF observed migrating. However, MFs were far from inactive, as they continuously extended and retracted dendrites (Movie S9), presumably sampling their immediate environment. We also routinely observed DCs scanning and interacting with MFs in the infiltrate (Fig. 4*D* and Movie S10). These stable interactions most frequently lasted 10–30 min (Fig. 4*E*).

In these established lesions, T cells continued to migrate freely and rapidly, as they had in the surrounding areas of the early

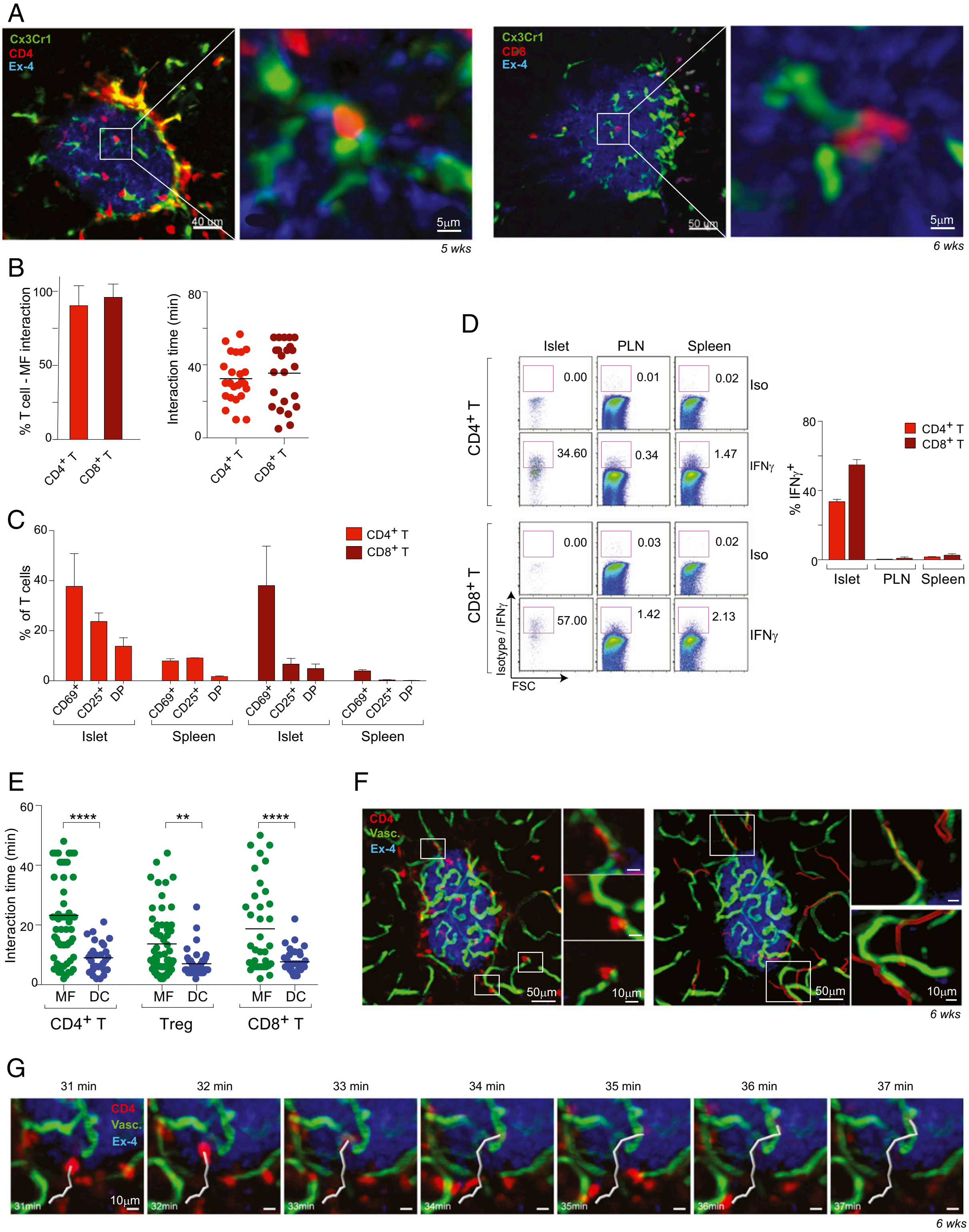

Fig. 3. Early T cell migration, interaction with APCs, and activation. (*A*) Representative time-lapse images depicting prolonged contact between T cells with islet resident MFs; white box indicates enlargements. (*B*) Quantitation of the overall proportion (*Left*) and duration (*Right*) of interactions between intraislet $CD4^+$ or $CD8^+$ T cells and islet resident MFs. (*C*) CD69 and CD25 expression on T cells from isolated islets and spleens of 5-wk-old NOD females; DP indicates frequency of cells expressing both CD69 and CD25. (*D*) IFN-γ expression in T cells restimulated ex vivo from isolated islets, pancreatic lymph nodes (PLN), or spleen. (*E*) Quantitation of early T cell interactions with MF and DC outside of the islet. (*F*) Representative IVM images depicting T cells associated with the vasculature (*Left*) and randomly selected examples of T cell migration tracks (*Right*). Boxes indicate regions shown at *Right*. (*G*) Representative time-lapse image series of a $CD4^+$ T cell migrating into an islet from the surrounding area. Error bars, SD. $^{**}P < 0.005$; $^{****}P < 0.0005$.

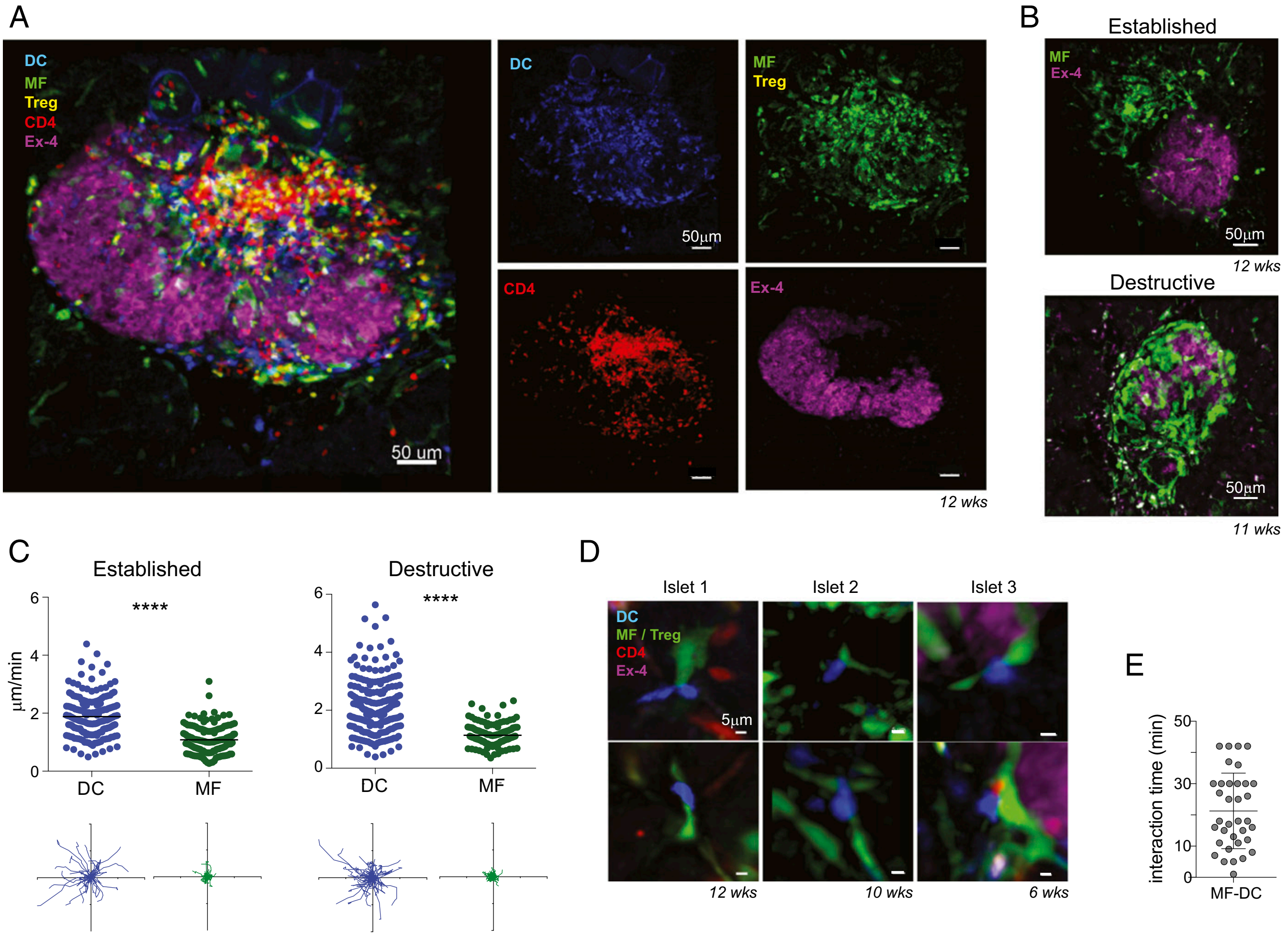

Fig. 4. MF and dendritic cell dynamics in advanced insulitic lesions. (*A*) Representative IVM image of multicellular florid insulitis in a 12-wk-old female *Cd4-tdTomato/Foxp3-GFP/Mertk-GFP/Flt3-BFP2* reporter mouse (*Left*); (*Right*) individual channels are shown. (*B*) Representative images illustrating the distribution of MFs in established insulitic lesions (*Upper*) and destructive lesions (*Lower*). (*C*) Quantitation of DC and MF migration velocities and displacement during established and destructive insulitic lesions. Flower plots represent migration over 10 min. (Scale bar, 50 µm.) (*D*) Images of inflamed islets from three independent mice depicting prolonged interactions between DC and MF. (*E*) Duration of MF/DC interactions. Data pooled from five mice. Error bars, SD. ***$P < 0.0005$.

lesions (mean velocities 5.4 ± 0.23 µm/min to 8.0 ± 0.24 µm/min) (Fig. 5*A* and Movies S11 and S12), even in the most advanced forms of destructive insulitis (Fig. 5*A*). T cells contacted both DCs and MFs, transiently for the most part (Fig. 5*B*), without the longer contacts with MFs that were noted in the earliest stages. In destructive lesions, CD8$^+$ T cells were less mobile (Fig. 5*A*, *Right*), with longer-lasting contacts with DCs (Fig. 5*B*, *Right*), and markedly higher arrest coefficients than CD4$^+$ T cells and Tregs (Fig. 5*C*). Accordingly, CD8$^+$ T cells showed higher expression of CD69, CD25, CXCR3, and IFN-γ than their CD4$^+$ counterparts (Fig. 5*D*), supporting the interpretation that these cells are strongly activated during this late phase of the disease process. We also noted, in these advanced lesions, that arrested Tregs were often in close association with CD8$^+$ T cells, much more frequently than with CD4$^+$ T cells (Fig. 5 *E* and *F* and Movie S13). These events of "coarrest" between Tregs and CD8$^+$ T cells, which were not observed in early and less-intense lesions, lasted 20 min on average. Together with the activated status of CD8$^+$ T cells, these events suggest that the terminal phases of islet destruction involve CD8$^+$ T cells more centrally than the earlier phases, and that Tregs may be responding to this differential activation status.

Discussion

A few studies have reported imaging analyses of pancreas autoimmunity in vivo at the cellular level (22, 23). The present work differs in several important respects that advance our understanding of the unfolding of T1D and help provide a context for previous observations. First, we imaged normal immunocytes, with a polyclonal repertoire that were naturally activated in vivo, over the course of a normal progression to T1D, instead of highly activated and monoclonal transgenic T cells in an acute transfer model (22, 23), which may have misrepresented the anatomical and cellular barriers that prevent T cells from rapidly overrunning pancreatic islets. Second, the unprecedented combination of knockin reporters, together with vascular tracers and β-cell–labeling nanoparticles, allowed us to visualize a ballet of many cell types in unison, following their movements and their interactions. While this system allows an unprecedented number of cells to be analyzed in concert, we acknowledge that some important players in the pathogenesis of diabetes, like B or NK cells, were not tracked. These characteristics combined to bring about unexpected dynamic pictures of DCs surveilling the lesions, T cells interacting stably with both MFs and DCs, and Tregs coarrested with CD8$^+$ T cells.

So, what do we learn about T1D pathogenesis from these data? In essence, these results provide a frame of reference into

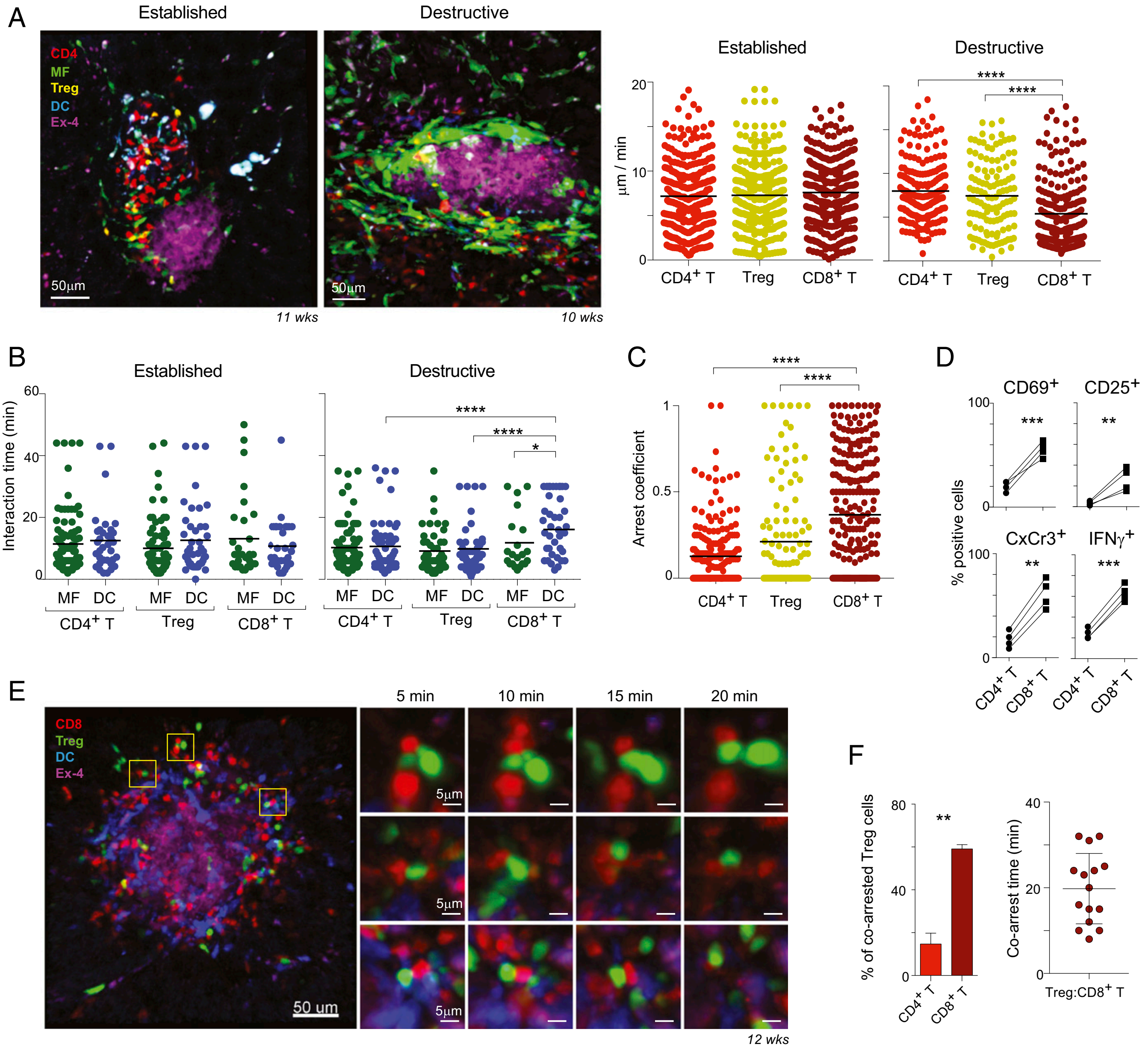

Fig. 5. T cell dynamics in advanced insulitic lesions. (*A*) Representative IVM images of established and destructive insulitis (*Left*) of bone-marrow–reconstituted female mice (20% *Cd4-tdTomato/Foxp3-GFP/Flt3-BFP2* and 80% *Mertk-GFP* input). Quantitation of T cell velocities within established and destructive insulitic lesions (*Right*). (*B*) Duration of T cell interactions with MF and DC within established and advanced lesions. (*C*) Arrest coefficients for different T cells within destructive insultic lesions. (*D*) Percentage, among $CD4^+$ or $CD8^+$ T cells from the pancreas of 12-wk-old NOD females, of cells expressing CD69, CD25, Cxcr3, and IFN-γ, as determined by flow cytometry. (*E*) Representative IVM image depicting Treg and $CD8^+$ T cell coarrest during destructive insulitis. Boxes indicate regions shown on *Right* over time. (*F*) Frequency and duration of Treg coarrest with $CD4^+$ or $CD8^+$ T cells. Data pooled from three to six female mice. Error bars, SD. *$P < 0.05$; **$P < 0.005$; ***$P < 0.0005$; ****$P < 0.0005$.

which the development and behavior of aggressive cell-types, and negative immunoregulatory cells, can be situated. We acknowledge that one cannot formally infer function from IVM observations. The cell dynamics and interactions suggest possible scenarios and cellular cross-talk, but it is not possible to infer specific functions (beyond those generally known for these populations). Similarly, although the literature and the $CD69^+$ status of the T cells being tracked suggest that most of them do recognize pancreatic antigens, we cannot infer any specificity from these images. Thus, some of the models we propose below are admittedly speculative.

At the onset of autoimmune progression, the data point to a previously unrecognized dichotomy between infiltrating cells that reside inside or outside the islet. These cells show very different behavior and dynamics: low mobility and very long interactions with MFs for those inside; high mobility and fewer interactions for those outside. The temporal course of T cell accumulation at early times (3–5 wk of age), with a drop in the proportion of cells inside the islet, suggests that the very first steps of autoimmune recognition may take place inside the islets, but that subsequent events unfold outside. The early T cells inside the islets may result from normal patrolling of the tissues, as they are also observed on the diabetes-resistant B6 × NOD genetic background, albeit less frequently and involving very few T cells. We cannot assert with certainty how these T cells enter the islets (extravasation across islet capillaries or migration from surrounding connective tissue), but the several examples of T cells entering the islets (Fig. 3*G*) suggest the latter. However, as our data do not capture the precise moment of initial attack, it cannot be determined how the very first lymphocytes actually invade the islet. Their numbers remain quite low (usually around 1–10 $CD4^+$ T cells per islet), indicating that there are strong barriers to intraislet accumulation of T cells in established insulitic lesions. This observation contrasts with several previous reports that showed massive entry of antigen-specific T cells into islets, but these studies involved donor T cells acutely activated in vitro, likely able to overcome normal barriers (22, 31). In NOD mice, these early infiltrating cells appear relevant to the process, in view of their frequent immobilization on APCs and highly activated phenotype. This conclusion is in keeping with demonstrations that colonization of islets requires a relevant TCR specificity (32, 33).

From there, the autoimmune lesions progress as a complex multicellular ensemble at the periphery of the remaining islet mass. Although some areas of preferential cellular localization were found (in particular, regions enriched in MFs or DCs), we did not observe, across the hundreds of islets imaged, clear cellular organization corresponding to tertiary lymphoid structures (11), and the multicellular infiltrates remained for the most part heterogeneous and geographically amorphous. Our previous analyses tracing NOD insulitis using the Kaede system would suggest that this cellular agglomeration is also open to the outside, receiving continuous input of fresh myeloid and lymphoid cells (34). Importantly, analysis of cell–cell interactions suggested the continued presentation of autoantigens by APCs in established insulitis of mice of all ages. Short-term (10- to 20-min duration) arrest of T cells were frequent, which involved both MFs and DCs as APCs. Very long-lasting T/APC interactions, such as those typically seen in LNs in the first 20 h of a synchronous activation of naïve T cells (35), were rare. However, since there was no sharp experimental starting point in the spontaneously infiltrated islets, most of the T cells present in the pancreatic infiltrate at any one time had already been activated in the preceding days or weeks.

We were surprised by the dynamic nature of DCs, most of which exhibited a high velocity and range, scouring the entire infiltrate area. This mobility contrasts with the described behavior of LN DCs which, with the exception of recently arrived migratory DCs, are essentially stationary (35). High mobility has an obvious functional grounding for T cells, which must patrol the organ space in search of their cognate antigens. This high mobility is not immediately obvious for DCs, which are devoid of such self/nonself recognition specificity. One might speculate that these highly mobile cells are sampling the space of the autoimmune lesion, likely following chemokine cues, before ferrying β-cell antigens to draining LNs. It is noteworthy that these DCs did not just swarm in or around the β-cell mass itself, but rather through the entire insulitis, indicating that structures or molecules from many cell types were being surveyed by the DCs, and perhaps captured for presentation. In a sense, the autoimmune lesion becomes self-referential.

In contrast to DCs, MFs were almost completely static, whether at the border of the islet or in the insulitic mass. Quite intriguing was the observation that mobile DCs arrested and formed stable contacts with these MFs. To our knowledge, such interactions have not been previously reported in IVM studies of any organ, likely because the combination of DC and MF reporters has not been used previously. We speculate that these DC/MF interactions may denote the transfer of antigens (as loaded MHC molecules) between MFs and DCs ("cross-dressing") (36). Antigen transfer has been reported for the gut, where luminal antigens captured by MFs are rapidly transferred to neighboring DCs (37). Such transmission would ensure the export to draining LNs of antigens preferentially captured and processed by immobile MFs.

In the most terminal lesions, the pictures of multicellular heterogeneity persisted, with several indications that the $CD8^+$ T cell compartment may be playing a more important role: longer arrest, more frequent activated phenotypes than for $CD4^+$ T cells, many images of "coarrest" together with Treg cells. This shift in dominance from $CD4^+$ to $CD8^+$ T cells would be consistent with the genetic control of T1D, whose principal determinism lies in MHC-II molecules, but with a secondary impact of genetic variants in MHC-I molecules that would affect $CD8^+$ T cells (38). Notably, both genetic and antibody-mediated ablation of $CD8^+$ T cells strongly protects from the development of diabetes (39–41).

In this overall framework, how might immunoregulation come into play? It is noteworthy that, even though presumably islet-specific T cells are congregating in and around the islets from a few weeks of age, their rate of amplification is somewhat modest compared with the expansion of $>10^5$-fold that can occur within a few days of viral infection. Treg cells are present at all stages and in all compartments, patrolling at high speed the same compartments as conventional $CD4^+$ T cells, consistent with the idea that Tregs constantly dampen the local autoimmune attack. Suppressive roles of MFs have also been reported (7), which may be accounted for by their position as gate-keepers to islet entry in the initial phases, or by the capsule that MFs appear to form around the remaining β-cell mass in cases of established insulitis.

Inflammation in islets of human patients has been hard to evaluate, given the challenging access to material. Most histological explorations have been done on pancreata from patients with overt, established T1D, weeks or months after onset, where accurate histological evaluation is complicated by ketoacidosis and variable handling of cadaveric samples (12). Only three truly prediabetic patients have been analyzed (42), making it difficult to relate the present observations during the preonset phases in the NOD mouse to human prediabetes. However, we note that images were observed in these prediabetic pancreata reminiscent of the advanced lesions of the NOD mouse, with heterogeneous cell populations involving both lymphoid and myeloid cells (42). In established T1D patients, a dominance of $CD8^+$ over $CD4^+$ T cells has been reported (13–15), which may correspond to the higher level of engagement by APCs and activation of $CD8^+$ T cells, relative to their $CD4^+$ counterparts, that we observed in the advanced NOD lesions. A recent study of infiltrating T cells in fresh pancreas specimens from patients at T1D onset showed a T cell infiltrate in all patients, which was predominantly at the periphery of the islets rather than inside (16), as in NOD mice. Overall, there is thus reason to think that the cellular dynamics and interactions observed here may have relevance to human T1D, or at least to some subtypes thereof. In conclusion, the "dynamic geography" of diabetes pathogenesis uncovered here provides a framework in which to analyze the cellular and molecular interactions during the unfolding of diabetes, as well as clues to immunoregulatory events that control it.

Materials and Methods

Mice and Treatments. NOD and NOD.*Foxp3-Ires-GFP* mice were bred under specific pathogen-free conditions in the Harvard Medical School animal facility. B6.129P-*Cx3cr1*^{tm1Litt}/J (JAX 5582) were back-crossed for 10 generations with NOD/LtJDoi. NOD.*CD4*^{tdtomato}, NOD.*CD8a*^{tdTomato}, NOD.*Mertk*^{GFPiDTR}, and NOD.*Flt3*^{iTagBFP2} were generated using CRISPR/Cas9 genome editing in isolated embryos from NOD mice. In certain instances, to reduce the number of label cells for imaging, we constructed mixed bone chimeras with differing proportions of reporter cells. Irradiated (10 Gy) 4- to 6-wk-old NOD females were reconstituted with a 8:2 mix of mixed bone marrow cells from $Mertk^{GFPiDTR}$ mice and either $CD4^{tdTomato}/Foxp3^{iGFP}/Flt3^{itagBFP2}$ or $CD8^{tdTomato}/Flt3^{itagBFP2}$ mice. All animal experiments were conducted in accordance to protocols approved by Harvard Medical School's and Massachusetts General Hospital's Institutional Animal Care and Use Committee.

Construction of Reporter Lines. Briefly, gene-targeting constructs containing fluorescent cassettes/ires/diphtheria toxin receptor and polyA terminator sequences were flanked by 5′ and 3′ homology arms consisting of 500 bp to 1 kb of homology on both ends. Linear template (2.0 ng/μL) DNA was coinjected with Cas9 mRNA (5 ng/μL; TriLink Biotechnologies) and a single sgRNA (2.5 ng/μL) into the pronucleus of isolated NOD embryos and reimplanted into surrogate Swiss-Webster recipients. Resulting offspring were screened for correct integration of targeting construct and for any modification of the native DNA sequence at the six most-likely off-target loci predicted by Bowtie software and online prediction tools (crispr.mit.edu).

Flow Cytometry. For cytometric analysis, cells were filtered through a 70-μm filter and washed before staining. Cells were stained in the presence of FC block for 30 min at 4 °C. To assess cytokine production, islets were isolated and dispersed as previously described (28), and were restimulated with PMA (10 ng/mL) and ionomycin (1 ng/mL) in the presence of a Golgi-plug for 3.5 h at 37 °C. Following surface staining, cells were fixed with 4% PFA, permeabilized with BD Perm/Wash, and stained intracellularly for cytokine detection. For analysis, stained cells were run on a LSR II flow cytometer (BD) and analyzed using FlowJo Software (TreeStar).

In Vivo Imaging Probes. Fluorescent Exendin-4 probes have been previously described (27). Briefly, a terminal cysteine residue was added to the carboxyl terminus of the 39-amino acid Exendin-4 synthetic peptide. The peptide was conjugated with SeTau 647-Maleimide (SETA BioMedicals) for 2 h, purified over Illustra NAP-5 Columns (GE Healthcare), and concentrated with 3-kDa centrifugal filters (EMD Millipore). Mice were injected with 100 pmol Ex4-SeTau 647 30 min before surgical procedures. To visualize the pancreatic vasculature network, 500 K MW dextran (Thermofisher) was conjugated to Pacific blue dye and injected into the tail vein during imaging.

Intravital Imaging. Before surgery, mice were initially anesthetized with ketamine (60 mg/kg; Bimeda)/xylazine (12 mg/kg; Putney) mixture and maintained with inhaled isoflourane (1–2% in 100% oxygen). To minimize pain, mice were administered with buprenorphine (0.1 mg/kg) 30 min before surgery. After shaving the left flank, a small longitudinal incision of the outer skin layer was made near the spleen. The outer skin layer was carefully separated from the peritoneal wall and surgically glued along the outer edges of the custom-designed imaging chamber. Subsequent cauterization of the peritoneal wall allowed access to the abdominal organs, including the pancreas. To avoid bleeding and the potential induction of experimental artifacts, internal organs were handled with soft cotton swabs and as minimally as possible. After minor dissection of connective tissue between the spleen and stomach, the spleen was carefully teased out of the abdominal cavity and onto the platform within the imaging chamber and secured in place with surgical glue (VetBond, 3M). The tail region of the pancreas was then exposed and gently covered with a glass coverslip to minimize tissue movement during imaging. The imaging chamber was filled with 37 °C Ringer's solution, completely submerging the spleen and pancreas, and connected to an autocontrolled, regulated heating element to maintain stable temperature control of the tissue throughout imaging. This approach effectively stabilized the pancreas, maintained physiologic vascular supply, and effectively allowed for the access to approximately one-half of the total pancreatic tissue for imaging.

Intravital time-lapse imaging was performed using a custom-modified Olympus FV1000 MPE laser-scanning microscope in both confocal and multiphoton modes. For confocal image acquisition, 405-, 473-, 559-, and 635-nm diode lasers were scanned sequentially with a DM405/473/559/635-nm dichroic beam splitter; emitted light was collected using combinations of beam splitters (SDM473, SDM560, and/or SDM 640) and emission filters BA430-455, BA490-540, BA575-620, and BA655-755 using a XLUMPLFLN 20× 1.0 NA water-immersion objective (Olympus). For multiphoton image acquisition a MaiTai DeepSee Ti:sapphire laser was tuned at 920 nm for excitation of GFP, tdTomato, and SeTau 647 and emitted light was collected using an XLPlan N 25× 1.05 NA water-immersion objective (Olympus). Individual imaging runs were typically 30–60 min in duration. Each *z*-stack would typically contain 11 optical sections, with a step size of 3–4 μm and an interval of 60 s or less.

Three-dimensional cellular tracking of individual cells was performed using Imaris (Bitplane) to calculate instantaneous velocity, mean velocity, track length, and displacement during the course of islet imaging. The arrest coefficient was calculated as a measure of cellular arrest and defined by the proportion of time the instantaneous velocity of a given cell was <2 μm/min. The number and identity of cell–cell contacts and the duration of these contacts was manually scored and confirmed by inspection of individual *z*-planes. Motion artifacts resulting from tissue drift or breathing effects was corrected using standard Imaris plugins. Images depicted in this report were processed with either Imaris or ImageJ software.

ACKNOWLEDGMENTS. We thank Claudio Vinegoni, Julia Schanin, Thorsten Mempel, and Uli von Andrian for help with experimental set-up and design and discussion; and L. Du for embryo microinjections. This work was supported in part by NIH Grants P01 AI054904 (to D.M., C.B., and R.W.) and R01EB010011 (to R.W.); and by the JPB foundation and a gift from the Howalt family (D.M. and C.B.). J.F.M. was supported by Fellowship 3-2014-216 from the Juvenile Diabetes Research Foundation.

1. Wållberg M, Cooke A (2013) Immune mechanisms in type 1 diabetes. *Trends Immunol* 34:583–591.
2. Anderson MS, Bluestone JA (2005) The NOD mouse: A model of immune dysregulation. *Annu Rev Immunol* 23:447–485.
3. Sitrin J, Ring A, Garcia KC, Benoist C, Mathis D (2013) Regulatory T cells control NK cells in an insulitic lesion by depriving them of IL-2. *J Exp Med* 210:1153–1165.
4. Serreze DV, et al. (1996) B lymphocytes are essential for the initiation of T cell-mediated autoimmune diabetes: Analysis of a new "speed congenic" stock of NOD. Ig μ null mice. *J Exp Med* 184:2049–2053.
5. Jansen A, et al. (1994) Immunohistochemical characterization of monocytes-macrophages and dendritic cells involved in the initiation of the insulitis and beta-cell destruction in NOD mice. *Diabetes* 43:667–675.
6. Ferris ST, et al. (2014) A minor subset of Batf3-dependent antigen-presenting cells in islets of Langerhans is essential for the development of autoimmune diabetes. *Immunity* 41:657–669.
7. Fu W, Wojtkiewicz G, Weissleder R, Benoist C, Mathis D (2012) Early window of diabetes determinism in NOD mice, dependent on the complement receptor CRIg, identified by noninvasive imaging. *Nat Immunol* 13:361–368.
8. Tan TG, et al. (2016) Identifying species of symbiont bacteria from the human gut that, alone, can induce intestinal Th17 cells in mice. *Proc Natl Acad Sci USA* 113: E8141–E8150.
9. Feuerer M, Shen Y, Littman DR, Benoist C, Mathis D (2009) How punctual ablation of regulatory T cells unleashes an autoimmune lesion within the pancreatic islets. *Immunity* 31:654–664.
10. Salomon B, et al. (2000) B7/CD28 costimulation is essential for the homeostasis of the CD4+CD25+ immunoregulatory T cells that control autoimmune diabetes. *Immunity* 12:431–440.
11. Lee Y, et al. (2006) Recruitment and activation of naive T cells in the islets by lymphotoxin beta receptor-dependent tertiary lymphoid structure. *Immunity* 25: 499–509.
12. In't Veld P (2011) Insulitis in human type 1 diabetes: The quest for an elusive lesion. *Islets* 3:131–138.
13. Willcox A, Richardson SJ, Bone AJ, Foulis AK, Morgan NG (2009) Analysis of islet inflammation in human type 1 diabetes. *Clin Exp Immunol* 155:173–181.
14. Coppieters KT, et al. (2012) Demonstration of islet-autoreactive CD8 T cells in insulitic lesions from recent onset and long-term type 1 diabetes patients. *J Exp Med* 209: 51–60.
15. Arif S, et al. (2014) Blood and islet phenotypes indicate immunological heterogeneity in type 1 diabetes. *Diabetes* 63:3835–3845.
16. Krogvold L, et al. (2016) Insulitis and characterisation of infiltrating T cells in surgical pancreatic tail resections from patients at onset of type 1 diabetes. *Diabetologia* 59: 492–501.
17. Friedman RS, et al. (2014) An evolving autoimmune microenvironment regulates the quality of effector T cell restimulation and function. *Proc Natl Acad Sci USA* 111: 9223–9228.
18. Schmidt-Christensen A, et al. (2013) Imaging dynamics of CD11c$^+$ cells and Foxp3$^+$ cells in progressive autoimmune insulitis in the NOD mouse model of type 1 diabetes. *Diabetologia* 56:2669–2678.
19. Miska J, et al. (2014) Real-time immune cell interactions in target tissue during autoimmune-induced damage and graft tolerance. *J Exp Med* 211:441–456.
20. Mahne AE, Klementowicz JE, Chou A, Nguyen V, Tang Q (2015) Therapeutic regulatory T cells subvert effector T cell function in inflamed islets to halt autoimmune diabetes. *J Immunol* 194:3147–3155.
21. Abdulreda MH, et al. (2011) High-resolution, noninvasive longitudinal live imaging of immune responses. *Proc Natl Acad Sci USA* 108:12863–12868.
22. Coppieters K, Amirian N, von Herrath M (2012) Intravital imaging of CTLs killing islet cells in diabetic mice. *J Clin Invest* 122:119–131.
23. Lindsay RS, et al. (2015) Antigen recognition in the islets changes with progression of autoimmune islet infiltration. *J Immunol* 194:522–530.
24. Yang H, et al. (2013) One-step generation of mice carrying reporter and conditional alleles by CRISPR/Cas-mediated genome engineering. *Cell* 154:1370–1379.
25. Calderon B, et al. (2015) The pancreas anatomy conditions the origin and properties of resident macrophages. *J Exp Med* 212:1497–1512.
26. Bettelli E, et al. (2006) Reciprocal developmental pathways for the generation of pathogenic effector TH17 and regulatory T cells. *Nature* 441:235–238.
27. Clardy SM, et al. (2014) Fluorescent exendin-4 derivatives for pancreatic β-cell analysis. *Bioconjug Chem* 25:171–177.

28. Calderon B, Suri A, Miller MJ, Unanue ER (2008) Dendritic cells in islets of Langerhans constitutively present beta cell-derived peptides bound to their class II MHC molecules. *Proc Natl Acad Sci USA* 105:6121–6126.
29. Vomund AN, et al. (2015) Beta cells transfer vesicles containing insulin to phagocytes for presentation to T cells. *Proc Natl Acad Sci USA* 112:E5496–E5502.
30. Bajénoff M, et al. (2006) Stromal cell networks regulate lymphocyte entry, migration, and territoriality in lymph nodes. *Immunity* 25:989–1001.
31. Calderon B, Carrero JA, Miller MJ, Unanue ER (2011) Cellular and molecular events in the localization of diabetogenic T cells to islets of Langerhans. *Proc Natl Acad Sci USA* 108:1561–1566.
32. Wang J, et al. (2010) In situ recognition of autoantigen as an essential gatekeeper in autoimmune CD8+ T cell inflammation. *Proc Natl Acad Sci USA* 107:9317–9322.
33. Lennon GP, et al. (2009) T cell islet accumulation in type 1 diabetes is a tightly regulated, cell-autonomous event. *Immunity* 31:643–653.
34. Magnuson AM, et al. (2015) Population dynamics of islet-infiltrating cells in autoimmune diabetes. *Proc Natl Acad Sci USA* 112:1511–1516.
35. Mempel TR, Henrickson SE, Von Andrian UH (2004) T-cell priming by dendritic cells in lymph nodes occurs in three distinct phases. *Nature* 427:154–159.
36. Wakim LM, Bevan MJ (2011) Cross-dressed dendritic cells drive memory CD8+ T-cell activation after viral infection. *Nature* 471:629–632.
37. Mazzini E, Massimiliano L, Penna G, Rescigno M (2014) Oral tolerance can be established via gap junction transfer of fed antigens from CX3CR1$^+$ macrophages to CD103$^+$ dendritic cells. *Immunity* 40:248–261.
38. Nejentsev S, et al.; Wellcome Trust Case Control Consortium (2007) Localization of type 1 diabetes susceptibility to the MHC class I genes HLA-B and HLA-A. *Nature* 450: 887–892.
39. Katz J, Benoist C, Mathis D (1993) Major histocompatibility complex class I molecules are required for the development of insulitis in non-obese diabetic mice. *Eur J Immunol* 23:3358–3360.
40. Serreze DV, Leiter EH, Christianson GJ, Greiner D, Roopenian DC (1994) Major histocompatibility complex class I-deficient NOD-B2mnull mice are diabetes and insulitis resistant. *Diabetes* 43:505–509.
41. Wang B, Gonzalez A, Benoist C, Mathis D (1996) The role of CD8+ T cells in the initiation of insulin-dependent diabetes mellitus. *Eur J Immunol* 26:1762–1769.
42. In't Veld P, et al. (2007) Screening for insulitis in adult autoantibody-positive organ donors. *Diabetes* 56:2400–2404.
43. Cong L, et al. (2013) Multiplex genome engineering using CRISPR/Cas systems. *Science* 339:819–823.
44. Wang H, et al. (2013) One-step generation of mice carrying mutations in multiple genes by CRISPR/Cas-mediated genome engineering. *Cell* 153:910–918.

Supporting Information

Mohan et al. 10.1073/pnas.1707381114

SI Materials and Methods

Mouse Generation. To create cellular reporters, we generated fluorescent knockin alleles targeting coding regions of endogenous genes. *Mertk*, *CD4*, and *CD8a* reporter alleles were designed to integrate directly following the ATG translation start site. The *Flt3* reporter allele was designed to integrate between the endogenous stop codon and the 3′UTR sequence. Constructs were cloned into TOPO PCR 2.1 vector backbone (Life Technologies) for long-term storage and sequencing. Before microinjection, targeting constructs were linearized by digest with EcoRV (New England Biolabs) and isolated by gel extraction (Qiagen).

For *CD4*, a 3.8-kb homology construct targeting exon 2 was generated comprised of the following sequence: 5′ homology arm (5′ HA, 1,043 bp, Chr 6:124880659–124879697, mm10) + ATG-tdTomato (1,431 bp)-TAA + Sv40 polyA Terminator (sv40 pA, 230 bp) + 3′ homology arm (3′ HA 1,081 bp Chr6:124879528–124878536, mm10). A double-strand DNA (dsDNA) break was induced by sgRNA guided Cas9 (guide seq-AGAGATGGCTCGGCACATGG, Cas9 cutting site Chr 6:124879654, mm10). Homologous recombination resulted in 49-bp deletion of the remainder of exon 2.

For *CD8a*, a 2.9-kb homology construct targeting exon 1 was generated comprised of the following sequence: 5′ HA, (594 bp, Chr 6: 71372958–71373551, mm10) + ATG-tdTomato (1,431 bp)-TAA + sv40 pA (230 bp) + 3′ HA (688 bp Chr6: 71373620–71374307, mm10). A dsDNA break was induced by sgRNA guided Cas9 (guide seq-GCGGGTCAACGGTGAGGCCA, Cas9 cutting site Chr 6: 71373557, mm10). Homologous recombination resulted in 64-bp deletion of exon 1 following the ATG codon.

For *Mertk*, a 3.4-kb homology construct targeting exon 1 was generated comprised of the following sequence: 5′ HA, (611 bp, Chr 2: 128698435–128699045, mm10) + ATG-eGFP (720 bp)-TAA +IRES (575 bp) + ATG-DTR-TGA (627 bp) + sv40 pA (230 bp) + 3′ HA (668 bp Chr2: 128699102–128699769, mm10). A dsDNA break was induced by sgRNA guided Cas9 (guide seq-CCAGAACCATCGCGGGGCCG, Cas9 cutting site Chr 2: 128699039, mm10). Homologous recombination resulted in 53-bp deletion of the remainder of exon 1.

For *Flt3*, a 2.5-kb homology construct targeting exon 24 was generated comprised of the following sequence: 5′ HA, (636 bp, Chr 5: 147331171–147331806, mm10) + ATG-tagBFP2 (702 bp)-TAA +IRES (575 bp) + 3′ HA (627 bp Chr5: 147330544–147331170, mm10). A dsDNA break was induced by sgRNA guided Cas9 (guide seq-GGAGAAAGAAGTTAGCGAGG, Cas9 cutting site Chr 5: 147331166, mm10).

sgRNAs were prepared according to previously published methods (43, 44).

Microinjection. Four- to 5-wk-old NOD females were injected with 2.5 IU PMSG followed by 2.5 IU HCG 47.5 h later. Superovulated females were set-up with stud males overnight and embryos were harvested the following morning from plugged females. sgRNA (2.5 ng/μL), Cas9 mRNA (5 ng/μL; TriLInk Biotechnologies), and linearized DNA template (2 ng/μL) were resuspended and mixed in 10 mM Tris/0.1 mM EDTA, pH 7.4 immediately before pronuclear injection. Resulting embryos were reimplanted into Swiss Webster surrogate recipients.

Flow Cytometry. Single-cell suspensions from spleens were generated by collagenase digestion. Minced spleen tissue was incubated in 1 mL DMEM-2% FBS + collagenase IV 1 mg/mL (Gibco), and DNaseI 10 U/mL (Sigma-Aldrich) at 37 °C for 20 min in a shaking incubator followed by physical dissociation through a 70-μm cell strainer (Falcon) and RBC lysis with ACK (Lonzo). Cells were stained for 20 min at 4 °C in FACS buffer (DMEM 2% FBS with Fc block). To distinguish different cell types present in the spleen the following gating strategies were used (corresponding data in Fig. 1*C*): CD4$^+$ T cells CD19$^-$ TCRb$^+$ CD4$^+$ *CD8*$^+$, T cells CD19$^-$ TCRb$^+$ CD8$^+$, B cells TCRb$^-$ CD19$^+$, NK cells CD19$^-$ B220$^-$ TCRb$^-$ Ly6g$^-$ F4/80$^-$ NKp46$^+$, g/d T cells CD19$^-$ B220$^-$ TCRb$^-$ Ly6g$^-$ F4/80$^-$ g/dTCR$^+$, *CD4*$^+$ *cDC* CD19$^-$ B220$^-$ TCRb$^-$ Ly6g$^-$ F4/80$^-$ CD11c$^+$ MHC-II$^+$ CD4$^+$ *CD8*$^+$, cDC CD19$^-$ B220$^-$ TCRb$^-$ Ly6g$^-$ F4/80$^-$ CD11c$^+$ MHC-II$^+$ CD8$^+$, pDC CD19$^-$ TCRb$^-$ Ly6g$^-$ F4/80$^-$ CD11c$^+$ B220$^+$ MHC-II$^+$, monocytes CD19$^-$ B220$^-$ TCRb$^-$ Ly6g$^-$ F4/80$^-$ CD11b$^+$ Ly6c$^+$, MFs CD19$^-$ B220$^-$ TCRb$^-$ Ly6g$^-$ CD11b^{int} CD11c^{int} AutoF^{hi} F4/80$^+$, neutrophils CD19$^-$ B220$^-$ TCRb$^-$ CD11b$^+$ Ly6g$^+$.

Islet Isolation. The pancreas was perfused with 5 mL islet buffer [HBSS + 1 mM $MgCl_2$ + 10 mM Hepes (Gibco) + 0.8 mg/mL Collagenase XI (Sigma-Aldrich)] via the common bile duct. Pancreata were excised and placed into siliconized vials with 2 mL islet buffer and digested at 37 °C for 12 min in shaking incubator. Digestion was terminated with the addition of 10 mL with cold wash buffer (islet buffer + 1 mM $CaCl_2$). Islets were washed three times and pelleted by centrifugation at 233 × *g* for 1 min. Islets were collected on 100-μm cell strainers (Falcon) and transferred into 60-mm Petri dishes with 25 mL cRPMI + 10% FBS. Islets were handpicked under a stereomicroscope and dispersed with 5 mL nonenzymatic cell dissociation solution (Sigma-Aldrich) at 37 °C for 10 min in a shaking incubator.

Pancreas Dispersion. For whole pancreas digestion, mice were perfused with 10 mL PBS via the left ventricle before organ harvest. Pancreata were dissected, minced, and subsequently incubated in 25 mL DMEM 2% FBS + collagenase IV 1 mg/mL (Gibco), and DNaseI 10 U/mL (Sigma-Aldrich) at 37 °C for 20 min in shaking incubator. To lyse RBCs, cells were resuspended with 1 mL ACK (Lonza) for 2 min on ice, washed, and filtered through a 70-μm cell strainer. Cells were stained on ice for 30 min at 4 °C in FACS Buffer (DMEM 2% FBS with Fc block) with antibodies against CD45, CD4, CD8, TCRβ, CD25, CD69, CxCr3, and IFN-γ (all antibodies from Biolegend).

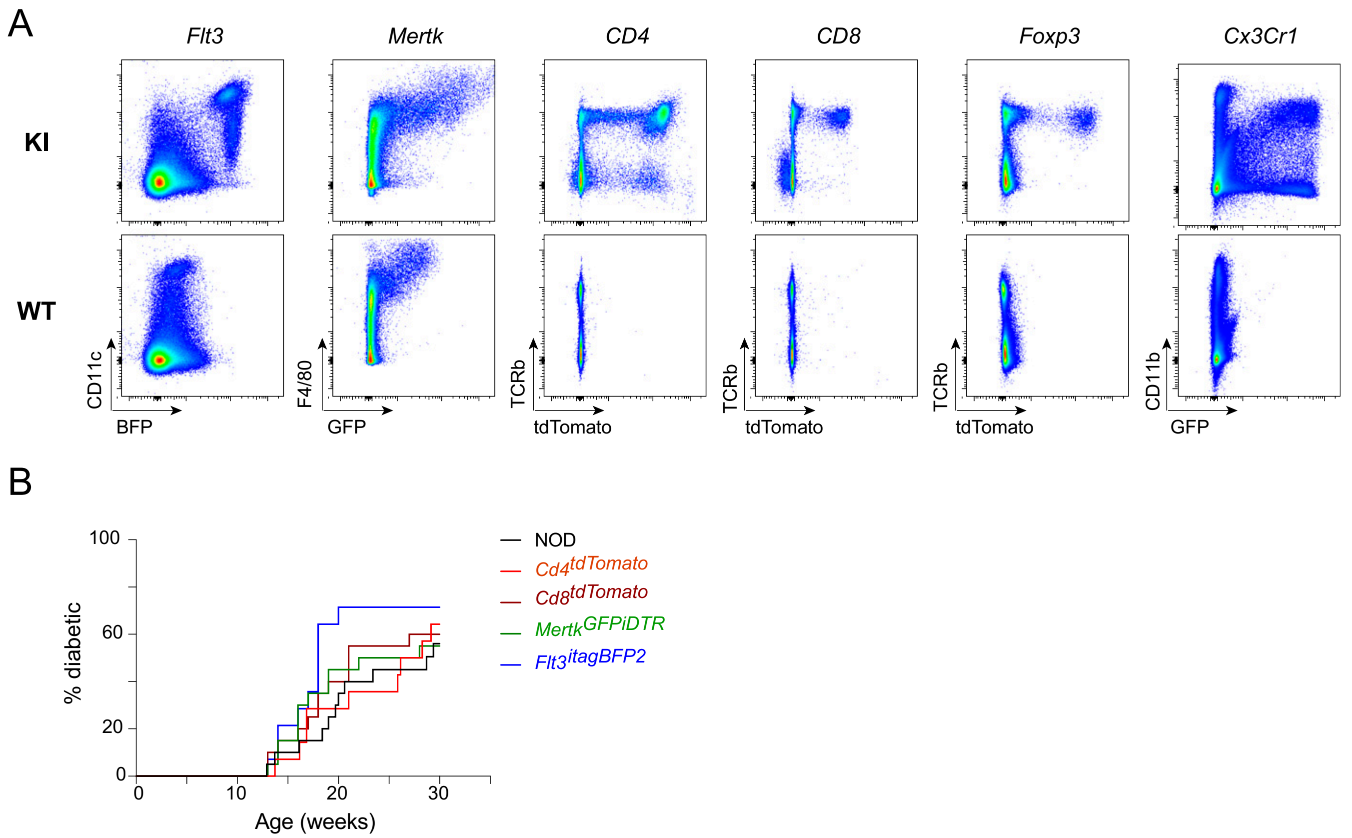

Fig. S1. Fluorescence profiles and diabetes incidence in NOD reporter lines. (*A*) Flow cytometric plots of KI (*Upper*) or WT (*Lower*) splenocytes depicting overview of fluorescence expression among total splenocytes. (*B*) Diabetes incidence in female NOD ($n = 20$), *CD4-tdTomato* ($n = 14$), *CD8a-tdTomato* ($n = 20$), *Mertk-GFP* ($n = 20$), and *Flt3-BFP2* ($n = 14$).

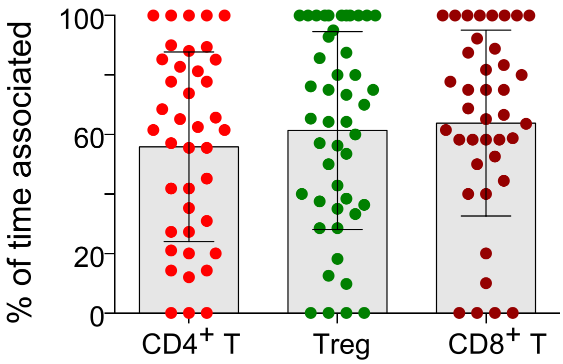

Fig. S2. Pancreas-infiltrating T cells migrate along the vascular network. T cells were analyzed for the proportion of time they were in contact with the endothelium during active migration.

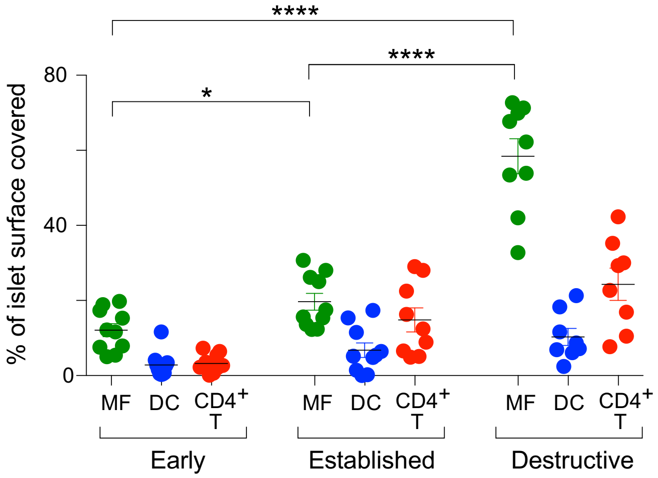

Fig. S3. Significant accumulation of MFs around the islet perimeter during destructive insulitis. The proportion of the islet perimeter surface area that was covered by either MFs, DCs, or CD4$^+$ T cells during the various stages of disease. *$P < 0.05$; ****$P < 0.0005$.

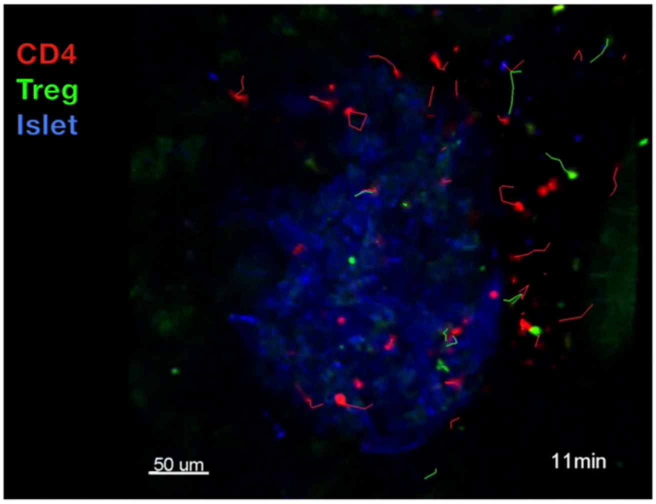

Movie S1. Early CD4$^+$ T cell migration within and around an infiltrated islet. Representative time-lapse imaging of CD4$^+$ T cell mobility during the early infiltration in a 5-wk-old *CD4-tdTomato-Foxp3-iGFP* mouse. Tracks represent the last five positions of the cell. Note the highly restricted mobility patterns of CD4$^+$ T cells and Tregs that are embedded within the islet compared with the more diffuse migration patterns of these cells in the space surrounding the islet. The movie corresponds with data shown in Fig. 2*D*.

Movie S1

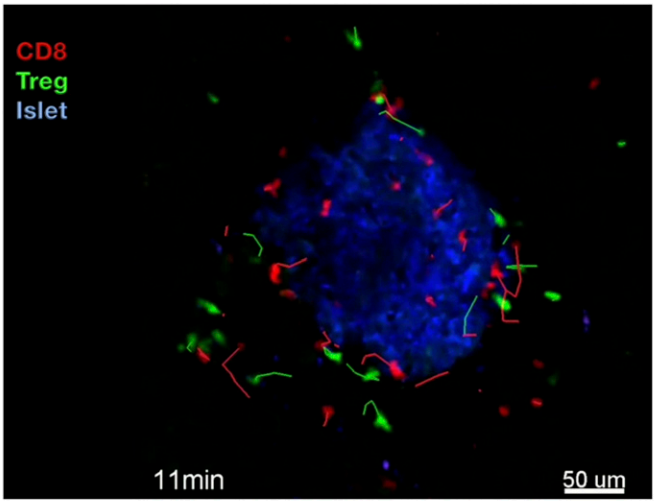

Movie S2. Early CD8$^+$ T cell migration within and around an infiltrated islet. Representative time-lapse imaging of T cell mobility during the early infiltration in a 5-wk-old *CD8a-tdTomato-Foxp3-iGFP* mouse. Tracks represent the last five positions of the cell. Note the highly restricted mobility patterns of CD8$^+$ T cells that are embedded within the islet compared with the more diffuse migration pattern of these cells in the space surrounding the islet. The movie corresponds with data shown in Fig. 2*D*.

Movie S2

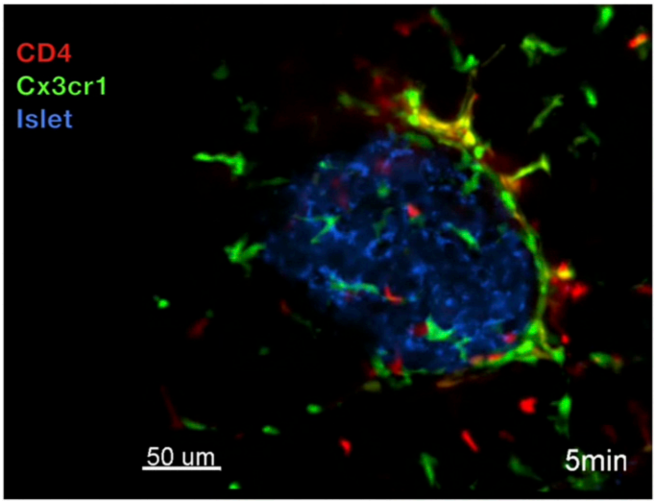

Movie S3. Early infiltrating CD4$^+$ T cells interact with islet resident MFs. Representative time-lapse imaging of sustained CD4$^+$ T cell–MF interactions within an islet of a 5-wk-old *CD4-tdTomato-Cx3cr1-GFP* mouse. The second part of the movie depicts a zoomed-in view of these interactions which occur in the defined region. Note that in this zoomed in representation the islet signal has been removed clarity. The movie corresponds with data shown in Fig. 3*B*.

Movie S3

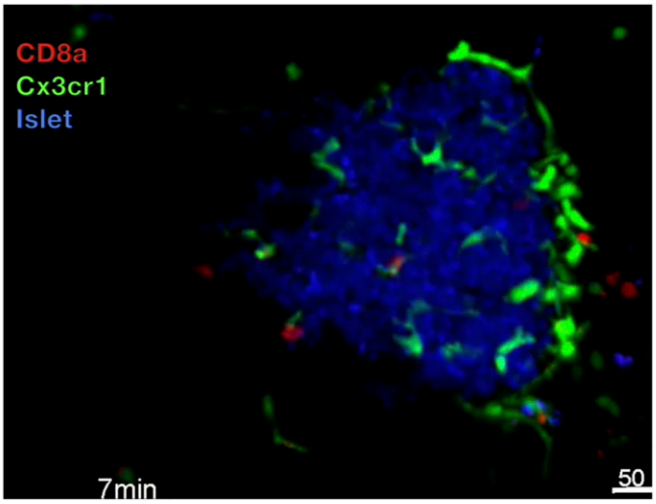

Movie S4. Early infiltrating CD8$^+$ T cells interact with islet resident MFs. Representative time-lapse imaging of sustained CD8$^+$ T cell–MF interactions within an islet of a 6-wk-old *CD8a-tdTomato-Cx3cr1-GFP* mouse. The second part of the movie depicts a zoomed-in view of these interactions occurring in the defined region. Note that in this zoomed-in version the islet signal has been removed clarity. The movie corresponds with data shown in Fig. 3*B*.

Movie S4

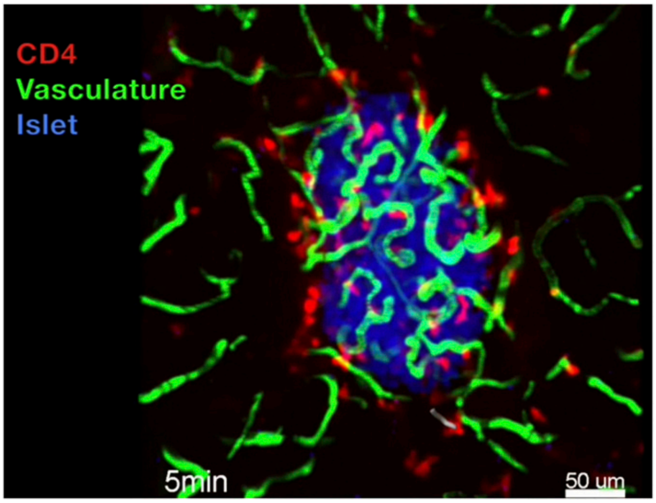

Movie S5. CD4$^+$ T cells migrate along the vasculature network. Representative time-lapse imaging of CD4$^+$ T cell migration in relationship to the pancreatic vasculature network in an infiltrated islet of a 6-wk-old *CD4-tdTomato* mouse. Pacific blue dextran (500 kDa) was injected intravenously 5 min before imaging to visualize the vasculature network. Example tracks from multiple T cells depict varying degrees of T cell migration along vasculature track. The movie corresponds with data shown in Fig. S2.

Movie S5

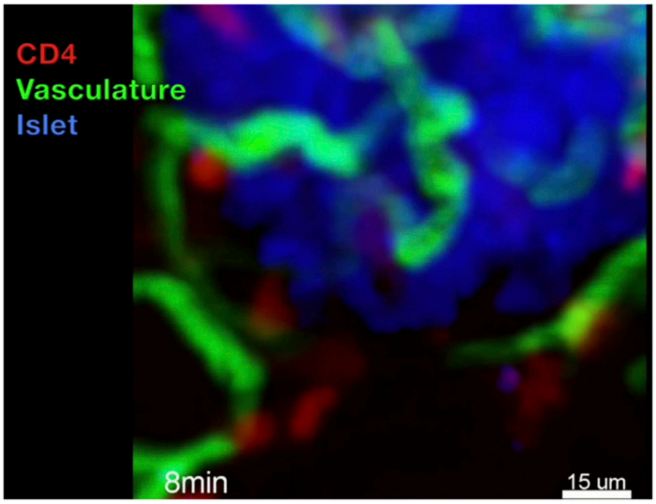

Movie S6. CD4$^+$ T cell migrating into an islet. Representative time-lapse imaging of a CD4$^+$ T cell (white track) migrating from the exocrine compartment into the islet of a 6-wk-old *CD4-tdTomato* mouse. The pancreatic vascular network was visualized by injection of 500 kDa Pacific blue dextran before imaging. The movie corresponds with data shown in Fig. 3*G*.

Movie S6

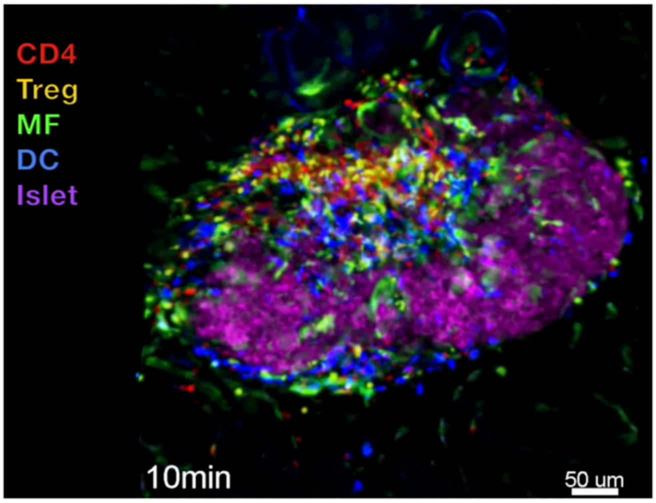

Movie S7. Advanced insulitis I. Representative time-lapse imaging of T cell, DCs, and MF dynamics during advanced insulitis in a 12-wk-old *CD4-tdTomato-Foxp3-iGFP-Mertk-GFP-Flt3-BFP2* mouse. In this particular lesion, which exhibits similarities akin to destructive insulitis defined by traditional H&E analysis (extensive cellular infiltrate, atypical "bowed" islet structure and appearance of cells invading into the islet), most of the T cell migration is occurs beyond the islet perimeter with intermittent traversing of CD4$^+$ T cells and Tregs over the top of islet. Note the significant accumulation of MFs and DCs and their close proximity to β-cells within advanced lesions.

Movie S7

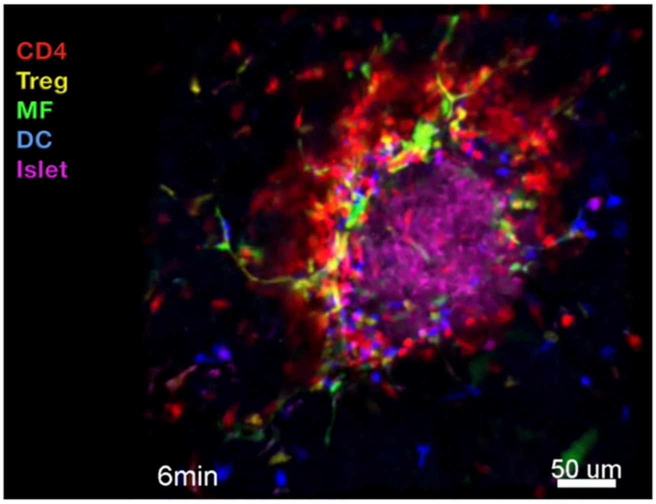

Movie S8. Advanced insulitis II. Representative time-lapse imaging of T cell, DCs, and MF dynamics during advanced insulitis in a 12-wk-old *CD4-tdTomato-Foxp3-iGFP-Mertk-GFP-Flt3-BFP2* mouse. In this particular lesion, which exhibits similarities akin to peri-insulitis defined by traditional H&E analysis (extensive cellular infiltrate, typical round structure, and appearance of cells completely confined to beyond the islet perimeter), there is a dense, actively mobile population of T cells that comprise the core insulitic lesion, which surrounds the islet. In addition, there is intermittent trafficking of T cells to and from the lesion which occurs through the exocrine compartment of pancreas. The second half of the movie depicts the same imaging series with signal from the *CD4-tdTomato* removed. Note the active migration behavior of the DCs, whereas the MFs are almost entirely sessile (migrating green cells were manually inspected and confirmed to be Tregs). The movie corresponds with data shown in Fig. 4*C*.

Movie S8

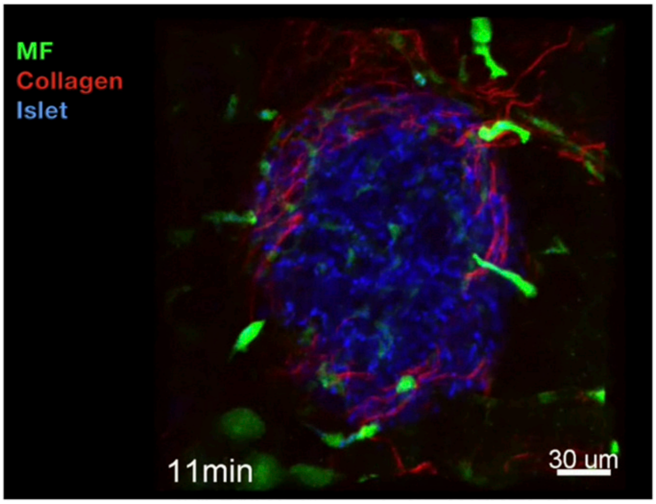

Movie S9. Homeostatic scanning of MFs in the pancreas of prediabetic mice. Representative time-lapse imaging of MFs and the collagen network (SHG) of an 8-wk-old *Mertk-GFP* mouse. MFs were largely sessile but actively surveyed their surroundings in the pancreas via dynamic projections.

Movie S9

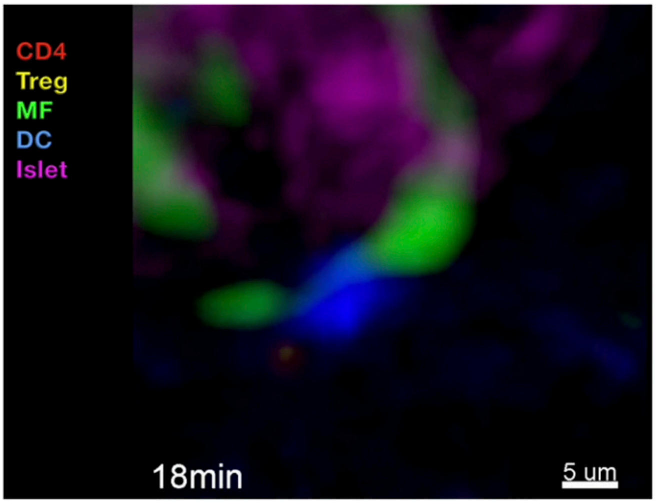

Movie S10. DCs interact with MFs. Representative time-lapse imaging of infiltrated islets from two independent mice, which show sustained DC/MF interactions of DCs both during early infiltration (6 wk old) and advanced infiltration (12 wk old) in *CD4-tdTomato-Foxp3-iGFP-Mertk-GFP-Flt3-BFP2* mice. The movie corresponds with data shown in Fig. 4*E*.

Movie S10

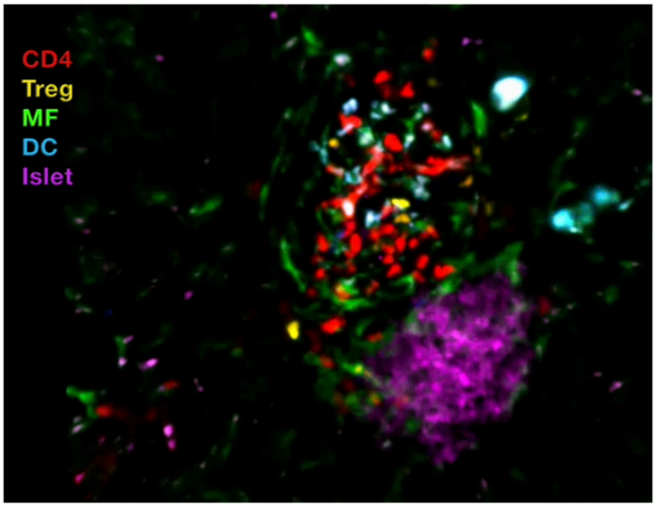

Movie S11. CD4$^+$ T cell migration during peri-insulitis. Time-lapse imaging of an infiltrated islet in a bone marrow chimeric mouse (input bone marrow cells: 80% from *Mertk-GFP* mice and 20% from *CD4-tdTomato-foxp3-iGFP-Flt3-BFP2* mice). Reducing the number of fluorescently labeled cells allows for more accurate tracking of T cell migration and interacts with APCs. In this representative peri-insulitic lesion, CD4$^+$ T cells and Tregs actively migrate through the lesion interacting often, but usually for only brief with MFs and DCs. Note the distribution of MFs, which are situated around the perimeters of the insulitic lesion. The movie corresponds with data shown in Fig. 5 *A* and *B*.

Movie S11

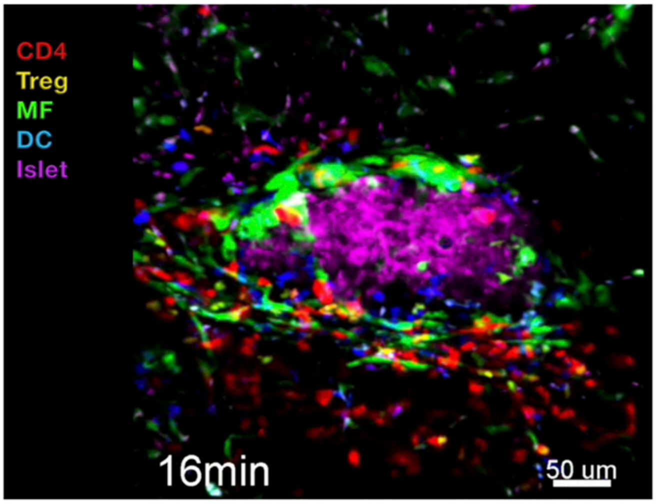

Movie S12. CD4$^+$ T cell migration during destructive-insulitis. Time-lapse imaging of an infiltrated islet in a bone marrow chimeric mouse (input bone marrow cells: 80% from *Mertk-GFP* mice and 20% from *CD4-tdTomato-foxp3-iGFP-Flt3-BFP2* mice). In this lesion, which resembles destructive insulitis, CD4$^+$ T cells and Tregs exhibit extensive motility while primarily only incteracting transiently with MFs or DCs. Note the significant accumulation of MFs in direct contact with β-cells residing at the islet perimeter. The movie corresponds with data shown in Fig. 5 *A* and *B*.

Movie S12

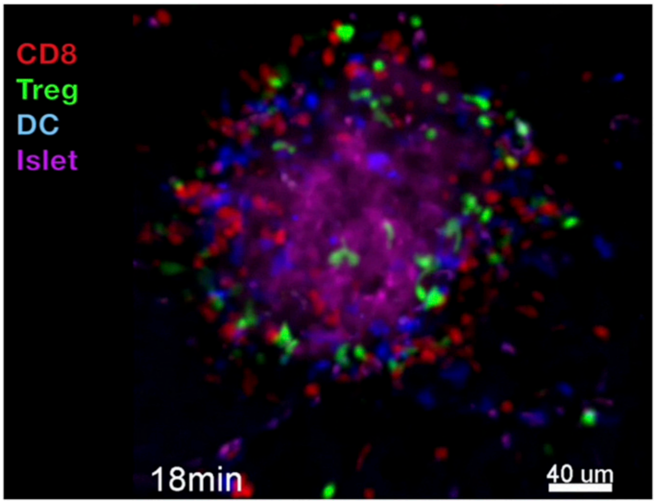

Movie S13. Coarrest of CD8$^+$ T cells and Tregs during destructive insulitis. Representative time-lapse imaging of destructive insulitis in a 12-wk-old *CD8a-tdTomato-Foxp3-iGFP-Flt3* mouse. During this advanced insulitis stage there is a striking arrest of CD8 T cells in the lesion. In addition, many Tregs were found coarresting with CD8 T cells. The movie corresponds with data shown in Fig. 5*F*.

Movie S13